A&A 489, 1–9 (2008)
DOI: 10.1051/0004-6361:200809699
© ESO 2008

Astronomy & Astrophysics

XMM-Newton studies of a massive cluster of galaxies: RXC J2228.6+2036

S. M. Jia[1,2], H. Böhringer[1], E. Pointecouteau[3], Y. Chen[2], and Y. Y. Zhang[4]

[1] Max-Planck-Institut für extraterrestrische Physik, 85748 Garching, Germany
e-mail: jiasm@ihep.ac.cn
[2] Key Laboratory of Particle Astrophysics, Institute of High Energy Physics, Chinese Academy of Sciences, Beijing 100049, PR China
[3] CESR-CNRS, 9 Av. du Colonel Roche, 31028 Toulouse, France
[4] Argelander-Institut für Astronomie, Rheinische Friedrich-Wilhelms-Universität Bonn, Auf dem Huegel 71, 53121 Bonn, Germany

Received 3 March 2008/ accepted 6 June 2008

ABSTRACT

We present the X-ray properties of a massive cluster of galaxies (RXC J2228.6+2036 at $z = 0.421$) using *XMM-Newton* data. The X-ray mass modeling is based on the temperature and density distributions of the intracluster medium derived using a deprojection method. We find that RXC J2228.6+2036 is a hot cluster ($T_{500} = 8.92^{+1.78}_{-1.32}$ keV) showing a cooling flow rate of $12.0^{+56.0}_{-12.0}$ $M_\odot$ yr^{-1} based on spectral fitting within the cooling flow radius ($r_{\rm cool} = 147 \pm 10$ kpc). The total cluster mass is $M_{500} = (1.19 \pm 0.35) \times 10^{15}$ $M_\odot$ and the mean gas mass fraction is $f_{\rm gas} = 0.165 \pm 0.045$ at $r_{500} = 1.61 \pm 0.16$ Mpc. We discuss the PSF-correction effect on the spectral analysis and find that, for the selected annular width, the PSF-corrected temperatures are consistent with those without PSF-correction. We observe remarkable agreement between X-ray and SZ results, which is of prime importance for future SZ surveys. RXC J2228.6+2036 obeys the empirical scaling relations found in general massive galaxy clusters (e.g. S–T, M–T, L–T and M–Y), after accounting for self-similar evolution.

Key words. galaxies: clusters: individual: RXC J2228.6+2036 – X-rays: galaxies: clusters

1. Introduction

The gravitational growth of fluctuations in the matter density distribution can be traced by the evolution of the galaxy cluster mass function (e.g. Schuecker et al. 2003). The hot and distant clusters are at the upper end of the mass distribution; they can therefore be used to probe the cosmic evolution of large-scale structure and are fundamental probes for cosmology. To date, few hot and distant clusters, however, have been detected. Therefore, it is important to study such clusters in detail, especially in X-ray.

RXC J2228.6+2036 is a distant ($z = 0.421$) and X-ray luminous cluster of galaxies in the northern sky. It is suspected to be massive and hot, and was well recognized as an extended X-ray source in the ROSAT All-Sky Survey, and included in both the NORAS galaxy cluster survey (Böhringer et al. 2000) and the ROSAT Brightest Cluster Sample (Ebeling et al. 2000).

The first combined SZ versus X-ray analysis for RXC J2228.6+2036 was based on SZ data from the Nobeyama Radio Observatory (NRO) 45 m radio telescope and the X-ray data from ROSAT/HRI. It shows that RXC J2228.6+2036 is a hot and massive cluster with $T = 10.4 \pm 1.8$ keV, $M_{\rm tot}(r < R_v = r_{178} = 2.9$ Mpc$) = (1.8 \pm 0.4) \times 10^{15}$ $M_\odot$, and a gas mass fraction of $f_{\rm gas} = 0.22 \pm 0.06$ (Pointecouteau et al. 2002). LaRoque et al. (2006) compared *Chandra* X-ray versus OVRO/BIMA interferometric SZ effect measurements for the same cluster, measuring $T = 8.43^{+0.78}_{-0.71}$ keV, $f_{\rm gas} = 0.138 \pm 0.009$ from the X-ray data, and $f_{\rm gas} = 0.188^{+0.035}_{-0.031}$ from the SZ data at r_{2500}. As one of the X-ray luminous galaxy clusters with both X-ray (*Chandra*) and SZ observations studied by Morandi et al. (2007), RXC J2228.6+2036 has a temperature of $T = 6.86^{+0.89}_{-0.71}$ keV and a total mass of $M_{\rm tot} = (4.90 \pm 4.35) \times 10^{14}$ $M_\odot$ at $r_{500} = 1033 \pm 464$ kpc. However, the above results are all based on the mass modeling under the assumption of isothermality of the ICM. The *XMM-Newton* EPIC instruments have high spatial and spectral resolutions and a large field of view, and are therefore suitable for completing a spatially resolved spectral analysis. We use *XMM-Newton* observations to a detailed study of RXC J2228.6+2036 based on X-ray mass modeling using a spatially resolved radial temperature distribution and perform a detailed X-ray versus SZ comparison.

The structure of this paper is as follows: Sect. 2 describes the data, background subtraction method, and spectral deprojection technique. Section 3 presents the spectral measurements using different models to derive the radial temperature profile, cooling time, and mass deposition rate. In Sect. 4, we show the radial electron density profile and X-ray mass modeling. In Sect. 5, we discuss the impact of the PSF correction on the spectral analysis, and compare the RXC J2228.6+2036 with SZ measurements and the empirical scaling relations for massive galaxy clusters. We draw our conclusions in Sect. 6.

Throughout this paper, unless explicitly stated otherwise, we use the 0.5–10 keV energy band in our spectral analysis. The cosmological model used is $H_0 = 70$ km s^{-1} Mpc^{-1}, $\Omega_{\rm m} = 0.3$, and $\Omega_\Lambda = 0.7$, in which $1'$ corresponds to 332.7 kpc at the distance of RXC J2228.6+2036.

2. Observation and data reduction

2.1. Data preparation

RXC J2228.6+2036 was observed for 26 ks in November 2003 by *XMM-Newton* and its observation ID is 0147890101. For

our purposes, we use only EPIC data (MOS1, MOS2 and pn). The observations were performed with a thin filter and in the extended full frame mode for pn and the full frame mode for MOS. Throughout this analysis, we use only the events with FLAG = 0, and with PATTERN ≤ 4 for pn and PATTERN ≤ 12 for MOS. The reduction was performed in SAS 7.1.0.

The light curve of the observation shows some flares (i) in the hard band (above 10 keV for MOS and above 12 keV for pn), possibly caused by the particle background; and (ii) in the soft band (0.3−10 keV), possibly due to episodes of soft proton flares (De Luca & Molendi 2004). Therefore, both the hard and the soft bands are used to select good time intervals (GTI) as described in Zhang et al. (2006). The GTI screening procedure provides 22 ks MOS1 data, 22 ks MOS2 data, and 18 ks pn data.

We applied the SAS task *edetect_chain* to detect the point sources (the radius of the point sources was 0.6′ containing 93% flux from the point source), and excised all of them from the cluster region. Then, a SAS command *evigweight* was used to create the vignetting weighted column in the event list to account for the vignetting correction for the effective area.

Due to read-out time delay, the pn data require a correction for the Out-of-time (OOT) events. We created the simulated OOT event file and used it to this correction (see Strüder et al. 2001) in our analysis.

2.2. Background subtraction

The *XMM-Newton* background consists of the following two components: i) particle background, which are high energy particles, such as cosmic-rays, that pass through the satellite, deposit a fraction of their energy on the detector, dominate at high energies, and show no vignetting; and ii) the Cosmic X-ray Background (CXB), which varies across the sky (Snowden et al. 1997), more important at low energies, and shows a vignetting effect.

We chose the blank sky accumulations in the Chandra Deep Field South (CDFS) as the background (Zhang et al. 2007), which was also observed with a thin filter. We applied the same reduction procedure to the CDFS data as to the cluster in the same detector coordinates, and the effective exposure time that we obtained for the CDFS data was 54 ks for pn, 61 ks for MOS1, and 61 ks for MOS2. RXC J2228.6+2036 is a distant cluster ($z = 0.421$); we estimated that the signal-to-noise ratio of the region $6' < R < 6.5'$ was about 20%, were able to assume approximately that the emission of the cluster covered only the inner part of the field of view ($R < 6'$). The outer region ($6.5' < R < 8'$) could therefore be used to monitor the residual background. We applied a double-background subtraction method to correct for these two types of background components as used in Arnaud et al. (2002). First, we estimated the ratio of the particle background, α, between RXC J2228.6+2036 and CDFS, from the total count rate in the high energy band (10−12 keV for MOS and 12−14 keV for pn), as described by Pointecouteau et al. (2004). S_0 and B_0 are the background spectra of the cluster and CDFS, respectively, in the region of $6.5' < r < 8'$ with area A_0, and S_i and B_i for spectra in the ith ring of the cluster and CDFS with area A_i. Then, after the double-background subtraction, the cluster spectrum $S(i)$ is (e.g. Jia et al. 2006; Zhang et al. 2006):

$$S(i) = S_i - \alpha B_i - \frac{A_i}{A_0}(S_0 - \alpha B_0). \quad (1)$$

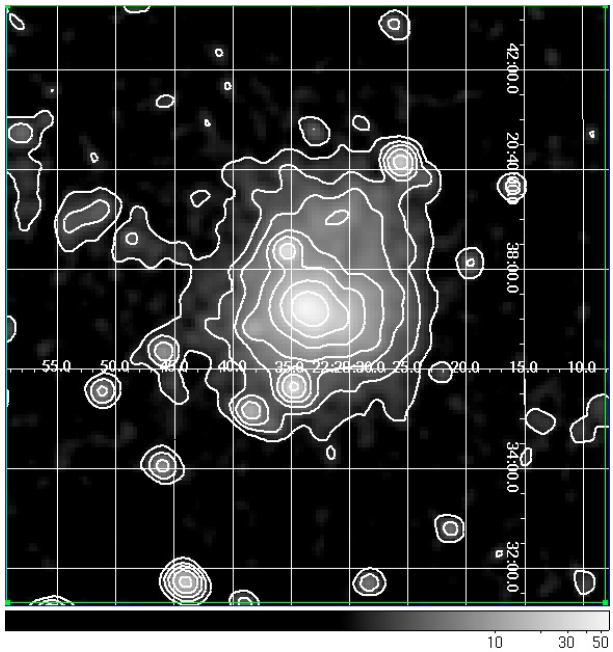

Fig. 1. The combined image of MOS1 and MOS2 of RXC J2228.6+2036 (12′ × 12′) corrected for vignetting and smoothed with a maximum Gaussian smoothing size of $\sigma = 5$ pixels.

2.3. Spectral deprojection

The combined image of MOS1 and MOS2 in the energy band 0.5−10 keV is shown in Fig. 1. It is corrected for vignetting and smoothed with a maximum Gaussian smoothing size of $\sigma = 5$ pixels. As shown in this figure, the X-ray emission of RXC J2228.6+2036 appears to be extended and almost symmetric apart from some bright point sources (which were subtracted before spectrum extraction, see Sect. 2.1). We extracted the spectra from annular regions centered on the emission peak, and the width of each ring was determined according to the criterion described in Zhang et al. (2007), ∼2000 net counts were extracted per bin at 2−7 keV energies to measure a temperature within a margin of error of ∼15%. Considering the PSF (Point Spread Function) effect of *XMM-Newton* EPIC, whose Full Width at Half Maximum (FWHM) is 5″ for MOS and 6″ for pn, the minimum width of each ring was set at 0.5′. We thus obtained 5 annuli to extract spectra out to 6′.

The deprojected spectra were calculated by subtracting all the contributions from the outer regions. Within each radial range, we assumed the same spectrum per unit volume. The deprojected spectrum of the ith shell was then calculated by subtracting the contributions from the $(i+1)$th shell to the outmost one (e.g. Matsushita et al. 2002; Nulsen & Böhringer 1995). The detailed calculation procedures were described in Jia et al. (2004, 2006):

$$D(i) = \left[S(i) - \sum_{k=i+1}^{N} C_v(k,i) \cdot D(k) \right] / C_v(i,i), \quad (2)$$

where $D(i)$ is the deprojected spectrum of the ith shell, $S(i)$ is the double-background subtracted spectrum of the ith shell, and $C_v(k,i)$ is the fraction of the volume of the kth shell projected to the ith ring.

The on-axis rmf (response matrix file) and arf (auxiliary responds file) are generated by the SAS task *rmfgen* and *arfgen* and are used to recover the correct spectral shape and normalization of the cluster emission components.

Table 1. The best-fit free parameters of RXC J2228.6+2036 for the single-temperature model: the temperature T, the abundance A, and the normalized constant *norm* for the simultaneously fitting of pn and MOS. $norm = 10^{-14}/(4\pi(D_A \times (1+z))^2) \int n_e n_H dV$, where D_A is the angular size distance to the source (cm) and n_e is the electron density (cm^{-3}). L_{bol} represents the bolometric luminosity (0.01−60 keV) in the units of 10^{44} erg s^{-1}. The errors represent a confidence level of 90%.

$r(')$	T (keV)	A (solar)	*norm* (10^{-3} cm^{-5})	χ^2_{red}/d.o.f.	L_{bol}(10^{44} erg s^{-1})
0.0−0.5	$8.26^{+1.02}_{-0.92}$	$0.31^{+0.19}_{-0.18}$	0.72 ± 0.03	1.12/251	$4.65^{+0.38}_{-0.31}$
0.5−1.0	$11.65^{+2.54}_{-1.78}$	$0.20^{+0.27}_{-0.2}$	0.88 ± 0.05	1.02/262	$6.73^{+0.58}_{-0.76}$
1.0−1.75	$9.03^{+1.82}_{-1.27}$	$0.30^{+0.25}_{-0.24}$	1.08 ± 0.06	1.00/196	$7.33^{+0.72}_{-0.74}$
1.75−3.0	$8.21^{+1.66}_{-1.26}$	$0.12^{+0.25}_{-0.12}$	1.28 ± 0.07	0.86/189	$7.89^{+0.81}_{-1.01}$
3.0−6.0	$5.10^{+5.68}_{-2.22}$	0.12(fixed)	$0.73^{+0.13}_{-0.10}$	0.51/59	$3.34^{+1.20}_{-1.96}$

3. Spectral analysis

3.1. Radial deprojected temperature profile

The spectral analysis was completed by using XSPEC version 11.3.2 (Arnaud 1996). To study the temperature distribution of RXC J2228.6+2036, we performed a joint fit to the spectra of pn and MOS with an absorbed Mekal model:

$$Model_1 = Wabs(N_H) \times Mekal(T, z, A, norm), \quad (3)$$

in which Wabs was a photoelectric absorption model (Morrison & McCammon 1983) and Mekal was a single-temperature plasma emission model (Mewe et al. 1985, 1986; Kaastra 1992; Liedahl et al. 1995). The temperature T, metallicity A, and normalization (emission measure) *norm* are free parameters. We fixed the redshift z to be 0.421 and the absorption N_H to be the Galactic value 4.68×10^{20} cm^{-2} (Dickey & Lockman 1990). The fitting results are listed in Table 1 and the central spectra fitted by this model are shown as Fig. 3a.

The deprojected temperature profile showed a drop in the core and a decrease in the outer regions (see the diamonds in the upper panel of Fig. 2), which could be fitted by the following formula (Xue et al. 2004):

$$T(r) = T_0 + \frac{A}{r/r_0} \exp\left(-\frac{(\ln r - \ln r_0)^2}{\omega}\right). \quad (4)$$

The best fit parameters were: $A = 4.880 \pm 0.001$ keV, $r_0 = 2.494 \pm 0.003'$, $\omega = 2.232 \pm 0.004$, $T_0 = 3.084 \pm 0.001$ keV, $\chi^2_{red} = 0.31$, and the best-fit profile is shown as the solid line in the upper panel of Fig. 2. From the temperature distribution, we can estimate the normalization-weighted temperature within 6′, $t_{mean} = 8.57^{+2.39}_{-1.56}$ keV, which is consistent with the results of Pointecouteau et al. (2002) and LaRoque et al. (2006) within the margins of error and a little higher than that of Morandi et al. (2007). The diamonds in the bottom panel of Fig. 2 show the deprojected abundance distribution of RXC J2228.6+2036.

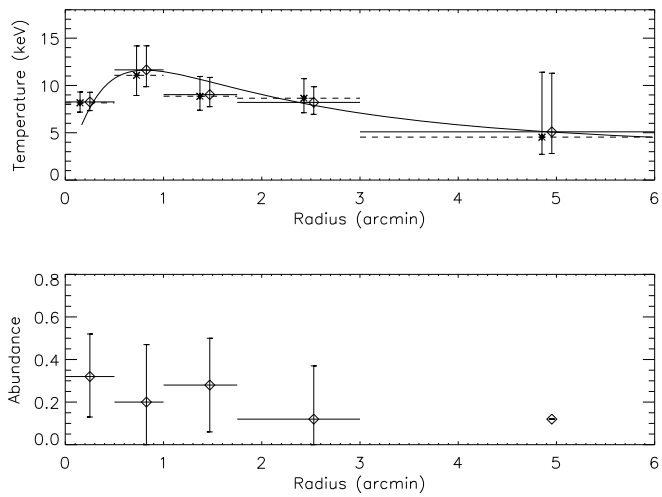

Fig. 2. *Upper panel*: radial temperature profile of RXC J2228.6+2036. Diamonds: the deprojected temperature and the solid line is the best-fit profile. Stars: for the PSF-corrected temperature (see Sect. 5.1). We offset the stars 5″ to the left so as to illustrate these two kinds of temperature clearly. *Bottom panel*: radial deprojected abundance of RXC J2228.6+2036. The confidence level is 90%.

3.2. Mass deposition rate

The temperature drop in the central part of RXC J2228.6 +2036 could indicate the existence of a cooling flow in the center. We thus estimate the parameters of the cooling flow as follows.

The cooling time t_{cool} is the timescale during which the hot gas loses all of its thermal energy, which is calculated to be (e.g. Chen et al. 2007):

$$t_{cool} = \frac{5}{2} \frac{n_e + n_i}{n_e} \frac{k_B T}{n_H \Lambda(T)}, \quad (5)$$

where $\Lambda(T)$ is the cooling function of the gas, and n_e, n_i, and n_H are the number densities of the electrons, ions, and hydrogen, respectively. For the almost fully ionized plasma in clusters, $n_e = 1.2 n_H$ and $n_i = 1.1 n_H$. The determination of n_e is explained in Sect. 4.1. The cooling time t_{cool} of the inner two regions is given in Table 2. The cooling radius designates the region inside which the hot gas loses all of its thermal energy within a cluster life timescale, which is usually assumed to be the age of the universe (1.04×10^{10} yr at $z = 0.421$). The resulting cooling radius for RXC J2228.6+2036 is $r_{cool} = 147 \pm 10$ kpc.

We also fit the central spectra of pn and MOS by adding a standard cooling flow model to the isothermal Mekal component:

$$Model_2 = Wabs(N_H) \times (Mekal(T, z, A, norm) + Zwabs(\Delta N_H) \times Mkcflow(\dot{M})), \quad (6)$$

where Wabs and Mekal were described in Sect. 3.1, Zwabs is an intrinsic photoelectric absorption model (Morrison & McCammon 1983), Mkcflow is a cooling flow model (Fabian 1988), ΔN_H is the intrinsic absorption, and $\dot{M}$ is the rate of gas cooling out of the flow. The fitting results show that the mass deposition rate in the central region $r < 0.5'$ is $14.0^{+64.0}_{-14.0}$ $M_\odot$ yr^{-1} (see Table 3); within r_{cool}, we therefore measure $\dot{M} = 12^{+56}_{-12}$ $M_\odot$ yr^{-1}. Figure 3b presents the central spectra fitted by this model.

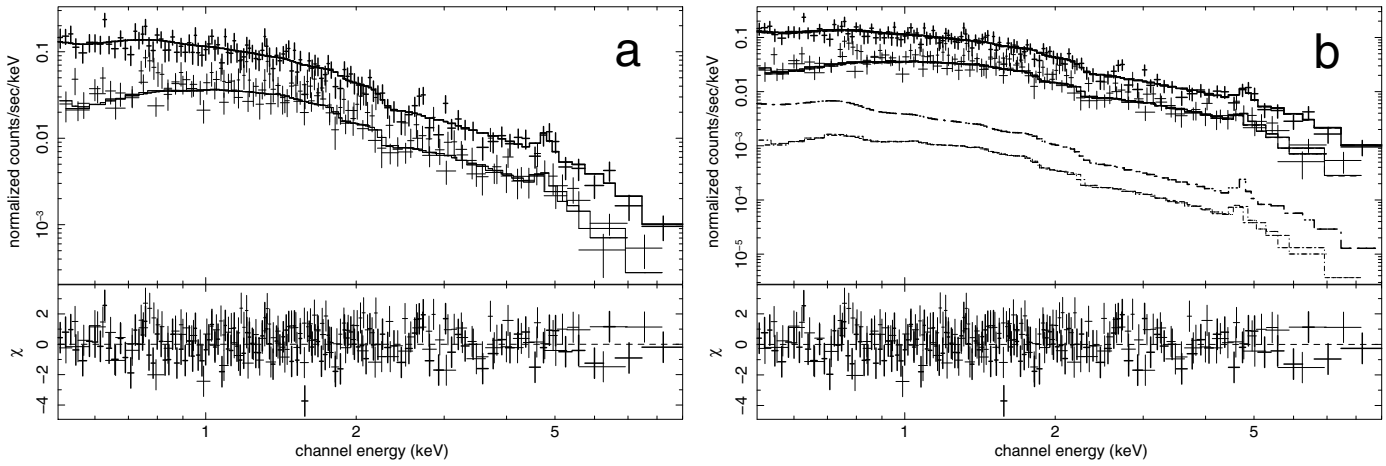

Fig. 3. The spectra of the central region ($r < 0.5'$) for joint fit of pn (bold crosses) and MOS (faint crosses) of RXC J2228.6+2036. **a)** Fitted by a single-temperature model; **b)** fitted by a cooling flow model with an isothermal Mekal component. In **b)** we plot the isothermal and the cooling flow components, and the lower lines below the crosses represent the multiphase components of pn (bold line) and MOS (faint lines), which show that the multiphase components provide only a small contribution to the emission.

Table 2. The cooling time and the cooling flow rate determined with the spatial method of the inner two regions of RXC J2228.6+2036. The errors are at the 68% confidence level. $1' = 332.7$ kpc.

r_1	r_2	$t_{\rm cool}$(yr)	$\dot{M}(M_\odot\ {\rm yr}^{-1})$
$0'$	$0.5'$	$1.18 \pm 0.07 \times 10^{10}$	200.2 ± 12.4
$0.5'$	$1'$	$3.58 \pm 0.27 \times 10^{10}$	414.7 ± 32.6

4. Mass determination

4.1. Electron density

We divided the $r < 6'$ region into 13 annuli centered on the emission peak, where the width of each annular region is determined to obtain at least 2000 total counts in each annulus region at 0.5−10 keV energies. After the vignetting correction and the double-background subtraction, the surface brightness profile for RXC J2228.6+2036, $S(r)$, was derived, which could be fitted by a double-β model (as Eq. (8)) convolved with the PSF matrices (Ghizzardi 2001) to correct for the PSF effect. Using the deprojection technique described in Sect. 2.3, we deprojected the double-β model (PSF corrected) and obtained the count rate of each corresponding shell, $Ctr(i)$. Since the temperature and abundance profiles were known, providing $T(i)$, $A(i)$ and $Ctr(i)$ in the ith shell, we could derive the corresponding $norm(i)$ in XSPEC with $Model_1$. The radial electron density $n_{\rm e}$ of each region could be determined from Eq. (7), shown as stars in Fig. 4.

$$norm(i) = 10^{-14}/(4\pi D^2) \cdot \int n_{\rm e} n_{\rm H} {\rm d}V. \quad (7)$$

We fitted the derived electron density (the stars in Fig. 4) with the double-β model (Chen et al. 2003):

$$n_{\rm e}(r) = n_{01}\left(1 + \left(\frac{r}{r_{\rm c1}}\right)^2\right)^{-\frac{3}{2}\beta_1} + n_{02}\left(1 + \left(\frac{r}{r_{\rm c2}}\right)^2\right)^{-\frac{3}{2}\beta_2}, \quad (8)$$

where the best-fit parameters were: $n_{01} = 0.0027 \pm 0.0002\ {\rm cm}^{-3}$, $r_{\rm c1} = 2.5480 \pm 0.0002$ arcmin, $\beta_1 = 1.4031 \pm 0.0001$, $n_{02} = 0.0109 \pm 0.0001\ {\rm cm}^{-3}$, $r_{\rm c2} = 0.6547 \pm 0.0004$ arcmin, $\beta_2 = 1.5474 \pm 0.0001$, $\chi^2_{\rm red} = 0.71$, d.o.f. = 7. The best-fit profile is shown as the solid line in Fig. 4.

4.2. Total mass

After measuring the radial temperature profile $T(r)$ and electron density profile $n_{\rm e}(r)$ for RXC J2228.6+2036, the integrated total mass of this cluster at radius r were calculated under the assumptions of hydrostatic equilibrium and spherical symmetry by the following equation (Fabricant et al. 1980):

$$M_{\rm tot}(<r) = -\frac{k_{\rm B} T r^2}{G\mu m_{\rm p}}\left[\frac{{\rm d}(\ln n_{\rm e})}{{\rm d}r} + \frac{{\rm d}(\ln T)}{{\rm d}r}\right], \quad (9)$$

where $k_{\rm B}$ is the Boltzmann constant, G is the gravitational constant, and μ is the mean molecular weight in units of the proton mass $m_{\rm p}$ (we assume $\mu = 0.6$ in this work). The mass uncertainties were obtained from the uncertainties in the temperature and the electron density calculated by MonteCarlo simulations. We obtained 250 redistributions of the parameterized temperature and electron density profiles by fitting data points that had been altered within the intervals defined by the Gaussian error bars of the measurements. The uncertainties in all the other properties of RXC J2228.6+2036 were also calculated from the 250 simulated clusters.

We then derived the total mass profile of RXC J2228.6+2036, shown in Fig. 5, and $M_{\rm tot} = (1.36 \pm 0.51) \times 10^{15}\ M_\odot$ at $6'$ at the 68% confidence level.

A physically meaningful radius for the mass measurement was defined to be r_{500}, the radius within which the mean gravitational mass density $\langle\rho_{\rm tot}\rangle = 500\rho_{\rm c}$, where $\rho_{\rm c} = 3H^2/(8\pi G)$ is the critical cosmic matter density. For our calculations, we used the value of $\rho_{\rm c}$ at the cluster redshift, i.e. $\rho_{\rm c} = 9.2 \times 10^{-30}\ {\rm g\,cm^{-3}}$. This radius was well covered by the observations. From the mass profile, we derived $r_{500} = 1.61 \pm 0.16$ Mpc for RXC J2228.6+2036, corresponding to $4.8' \pm 0.5'$, and the total mass within this radius was about $M_{500} = (1.19 \pm 0.35) \times 10^{15}\ M_\odot$. The mass derived from *Chandra* data by Morandi et al. (2007) was $M_{\rm tot} = (4.90 \pm 4.35) \times 10^{14}\ M_\odot$ within $r_{500} = 1033 \pm 464$ kpc, which is consistent with our measurement within the margins of error. In our analysis, the extrapolated value of $r_{\rm vir} = 2.48 \pm 0.38$ Mpc $= 7.5' \pm 1.1'$, and $M_{\rm vir} = (1.55 \pm 0.72) \times 10^{15}\ M_\odot$, which both agree with the measurements derived by Pointecouteau et al. (2002).

Table 3. The best-fit parameters for the central region of RXC J2228.6+2036 by $Model_2$. The $lowT$ is fixed on 0.01 keV and 1′ = 332.7 kpc. The errors are at the 90% confidence level.

r	$T_{\rm mekal}$ (keV)	Low $T_{\rm cf}$ (keV)	High $T_{\rm cf}$ (keV)	A (solar)	Norm (10^{-3} cm^{-5})	$\dot{M}$ ($M_\odot$)	$\Delta n_{\rm H}$ (10^{22} cm^{-2})	$\chi^2_{\rm red}$/d.o.f.
0′–0.5′	$8.54^{+2.27}_{-1.18}$	0.01 (fix)	$=T_{\rm mekal}$	0.32 ± 0.19	$0.70^{+0.05}_{-0.12}$	$14.0^{+64.0}_{-14.0}$	0.0(fix)	1.12/250

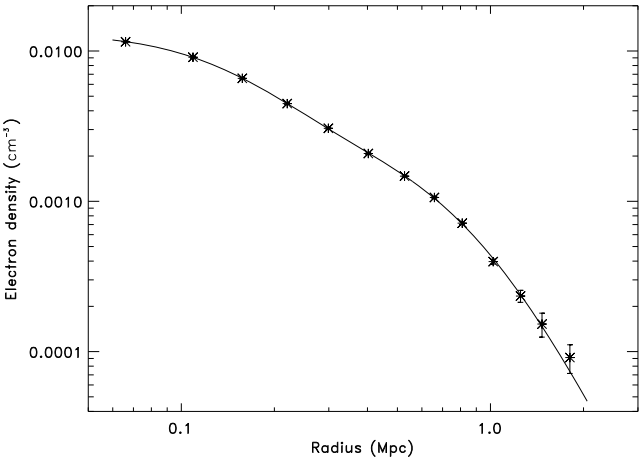

Fig. 4. The deprojected electron density profile of RXC J2228.6+2036 after PSF correction. The error bars are at the 68% confidence level. The solid line is the best-fit profile from a double-β model fitting.

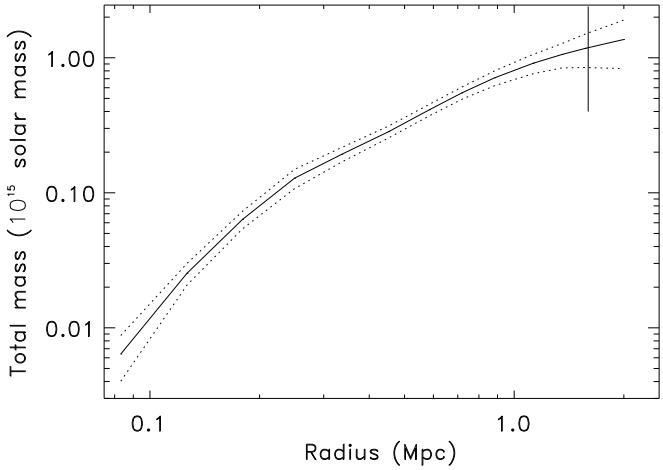

Fig. 5. The total mass profile of RXC J2228.6+2036, and the error bars (dotted lines) are at the 68% confidence level. The vertical line indicates r_{500} = 1.61 ± 0.16 Mpc.

4.3. Gas mass and gas mass fraction

In galaxy clusters, gas is an important component that is described by complex physical models. From the electron density, we calculated the gas mass and the gas mass fraction defined $f_{\rm gas}(r) = M_{\rm gas}(r)/M_{\rm tot}(r)$. Figure 6 shows the gas mass fraction profile of RXC J2228.6+2036. The gas mass fraction at 6′ was $f_{\rm gas}$ = 0.17 ± 0.06, consistent within the error bars with the results of LaRoque et al. (2006) from the *Chandra* X-ray and OVRO/BIMA interferometric SZ effect measurements, $f_{\rm gas}$ = 0.138 ± 0.009 from the X-ray data and $f_{\rm gas} = 0.188^{+0.035}_{-0.031}$ from the SZ data. It also agrees with the WMAP measured baryon fraction of the Universe $f_{\rm b} = \Omega_{\rm b}/\Omega_{\rm m}$ = 0.166 (Spergel et al. 2003).

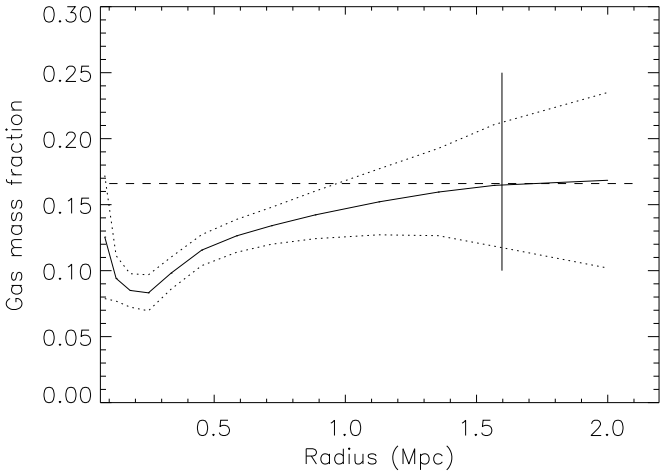

Fig. 6. The gas mass fraction profile of RXC J2228.6+2036. The dashed horizontal line indicates the WMAP measurement of $f_{\rm b} = \Omega_{\rm b}/\Omega_{\rm m}$ = 0.166 (Spergel et al. 2003) and the vertical line indicates r_{500} = 1.61 ± 0.16 Mpc. The error bars (dotted lines) represent those of the 68% confidence level.

5. Discussion

5.1. PSF-corrected spectra

The spatially resolved spectral analysis is affected by the PSF. To correct for the PSF effect, we first calculated the redistribution matrix F_{ij}, which is the fractional contribution of the ith ring originating in the jth ring (Pratt & Arnaud 2002). We derived this redistribution from our best-fit double-β model of electron density (converted to emission measure profile) and the PSF matrices (Ghizzardi 2001). Since we divided our cluster into 5 regions, we were able to obtain the fractional contribution of each ring originating in all bins, and in Fig. 7, we plot the contributions from the bin, all inner and outer bins.

Here, O_i is the observed spectrum of the ith ring after a double-background subtraction, S_i is the spectrum that is unaffected by the PSF; for our cluster RXC J2228.6+2036, we therefore have:

$$\begin{pmatrix} F_{11} & F_{12} & F_{13} & F_{14} & F_{15} \\ F_{21} & F_{22} & F_{23} & F_{24} & F_{25} \\ F_{31} & F_{32} & F_{33} & F_{34} & F_{35} \\ F_{41} & F_{42} & F_{43} & F_{44} & F_{45} \\ F_{51} & F_{52} & F_{53} & F_{54} & F_{55} \end{pmatrix} \cdot \begin{pmatrix} S_1 \\ S_2 \\ S_3 \\ S_4 \\ S_5 \end{pmatrix} = \begin{pmatrix} O_1 \\ O_2 \\ O_3 \\ O_4 \\ O_5 \end{pmatrix}. \quad (10)$$

From this function we derived S_i, which corresponded to the spectra after PSF correction. We then deprojected these spectra S_i by the deprojection technique described in Sect. 2.3, and derived the PSF-corrected deprojected spectra. Fitting these

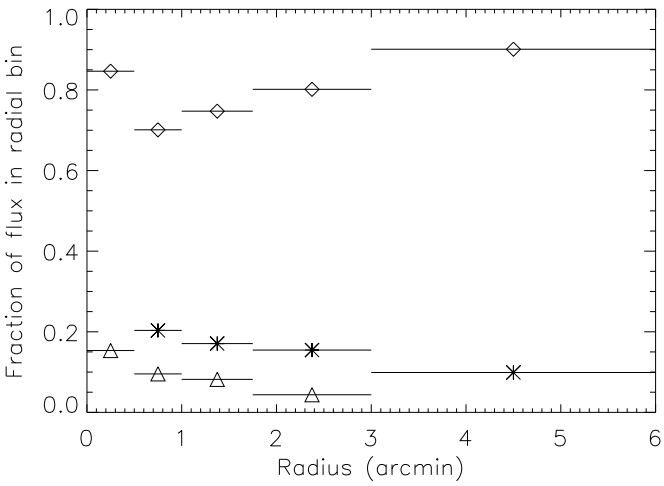

Fig. 7. Redistributions due to the *XMM-Newton* PSF: the diamonds represent the contribution coming from the bin, the stars from the inner bins and the triangles from the outer bins.

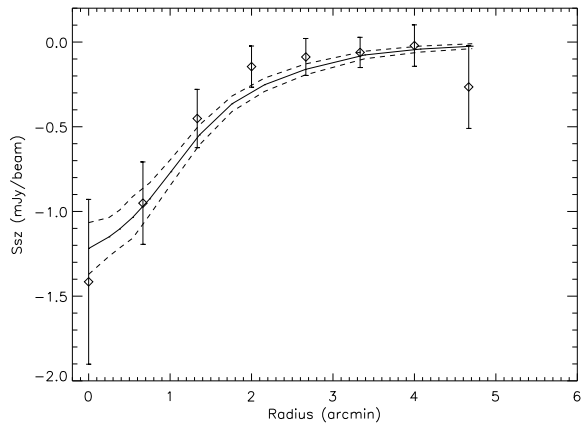

Fig. 8. The integrated X-ray pressure profile of RXC J2228.6 +2036 convolved with the PSF of the SZ telescope (the solid line) and compared with the SZ radial profile (the diamonds) derived by Pointecouteau et al. (2002). All errors shown correspond to the 68% confidence level.

spectra with $Model_1$, we obtained the PSF-corrected deprojected temperatures, shown as stars in the upper panel of Fig. 2.

We found that the PSF-corrected temperatures agreed with the measurements before the PSF-correction. This may be due to the broad width of the regions that we chose. However, it should be noted that these spectral fits are not as good as those in Sect. 3.1 because the PSF-correction procedure introduces significant uncertainties, mainly due to the inversion process (see Eq. (10)).

5.2. Gas pressure and comparison with the SZ data

With the temperature profile $T(r)$ and electron density profile $n_e(r)$, we derived the gas pressure profile of RXC J2228.6+2036 to be:

$$P(r) = n_e(r) k_B T(r). \tag{11}$$

In terms of observables, the gas pressure can be checked against the SZ effect (Sunyaev & Zel'dovich 1972) coming from the cluster. Indeed the SZ effect is directly proportional to the integrated pressure over the line of sight:

$$\begin{aligned} S_{SZ}(r) &= \frac{\sigma_T}{m_e c^2} \int k_B T(r) n_e(r) \mathrm{d}r \cdot f_{SZ}(v, T) \\ &= \frac{\sigma_T}{m_e c^2} \int P(r) \mathrm{d}r \cdot f_{SZ}(v, T), \end{aligned} \tag{12}$$

where k_B, m_e, c and σ_T are the Boltzmann constant, the electron mass, the speed of light and the Thomson cross-section; $f_{SZ}(v, T)$ represents the SZ spectral shape (including the relativistic corrections as computed by Pointecouteau et al. 1998).

Here we integrated the gas pressure of RXC J2228.6 +2036 using Eq. (12), convolved with the PSF of the 45 m radio telescope NRO (the beam size at 21 GHz: $\theta_{FWHM} \sim 80$ arcsec), and then compared its value with the SZ radial profile of gas pressure (Pointecouteau et al. 2002) in Fig. 8. The diamonds are from the SZ data and the solid line represents our result. We found remarkable agreement between the measurements within the margins of error.

The good agreement between the X-ray and SZ surface brightness profiles in Fig. 8 could allow us to check for biases in the derivation of the pressure profile from the X-ray data. The most interesting aspects concern a bias in temperature measurement in the presence of a multi-temperature ICM (e.g. Mazzotta et al. 2004; Vikhlinin 2006) and the overestimate of gas density due to the enhancement in surface brightness if the gas is clumpy. We now will investigate how these two effects modify the comparison between the X-ray and SZ data.

If we assume that the ICM is in approximate pressure equilibrium, the two bias effects on the temperature and the density are linked (for $n_e \times T$ = const.). While local unresolved density inhomogeneities correspond to an overestimation of the density and the prediction of a SZ-signal that is too high, the temperature of a clumpy medium will be underestimated in contrast to a mass average one and result in an underprediction of the SZ signal. Both effects at least partly compensate each other in our study.

Quantitatively, the overestimation of the gas density is given by:

$$C' = \frac{\langle n_e^2 \rangle}{\langle n_e \rangle^2}, \tag{13}$$

where the overestimation factor is $C = \sqrt{C'}$. To quantify approximately the underestimation of the temperature for this hot cluster, we can use the approach of Mazzotta et al. (2004, Eq. 14) which yields:

$$\frac{T_{sl}}{T} = R = \frac{\langle n_e \rangle \langle n_e^{1.75} \rangle}{\langle n_e^{2.75} \rangle}, \tag{14}$$

where T_{sl} is a good approximation of the spectroscopic temperature as would be obtained from data analysis of *Chandra* and *XMM-Newton* observations for a multi-temperature plasma, and T the mass-weighted mean.

As an example, we calculate these effects for a homogeneous distribution with a lower and higher cutoff of $T_1 = \langle T \rangle - \varepsilon$ and $T_2 = \langle T \rangle + \varepsilon$, respectively. A more general distribution can also be described by a superposition of many of these top-hat distributions. Figure 9 shows the enhancement factors C and R as a function of the distribution width parameter, ε. We note that the two bias effects that we study do not cancel the effects of each other, but the influence of the temperature underestimate is about 2−3 times larger than the overestimat due to clumpiness.

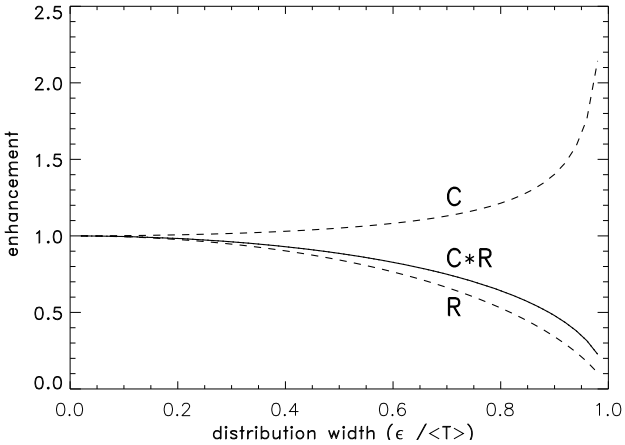

Fig. 9. Overestimation factor of the gas density C and underestimation of the spectroscopic-like temperature versus the mass-weighted temperature R as a function of the width of a homogeneous temperature distribution in the presence of pressure equilibrium. The combined effect $C \times R$ is for the underestimation of SZE. For the definition of the parameters see the text.

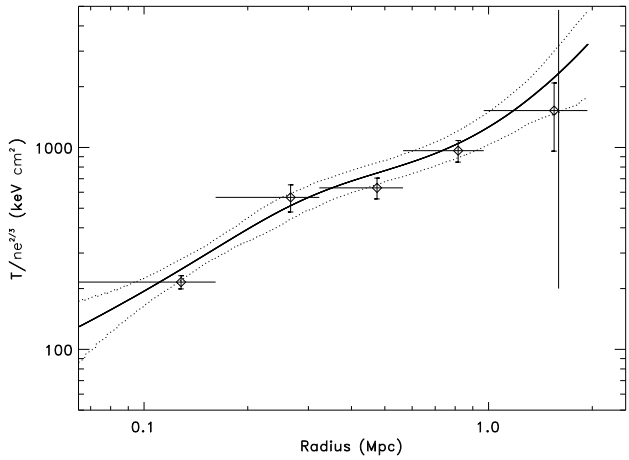

Fig. 10. The entropy distribution of RXC J2228.6+2036. The diamonds represent the entropy derived from the spectral fitting results and the solid line from the best-fit $T(r)$ and $n_e(r)$ profiles. The vertical line shows $r_{500} = 1.61 \pm 0.16$ Mpc. The error bars are at the 68% confidence level.

However, the overall effect is not dramatic and does not provide a very good diagnostics. Even for a broad temperature distribution with $\varepsilon/\langle T\rangle \approx 0.75$ for example, covering a temperature range (from the lower temperature to the higher temperature) of a factor of 7, we obtain an SZE underestimate of about 30% and a gas mass overestimate of about 18%.

This has also implications on the mass measurement. While the pressure profile and its derivative can be obtained directly from the SZ-profile, we still require an independent absolute temperature measurement for the normalization of the mass profile. The above calculation illustrates, that we do not obtain significantly more information about a possible bias in temperature to lower values due to a multiphase ICM, from the analysis of simultaneous X-ray and SZ observations. In the above example, a temperature and mass underestimation of 40% is indicated only by an SZ deviation of 30%.

5.3. Gas entropy and the S – T relation

Following Ponman et al. (1999), we defined the entropy of the gas in clusters to be:

$$S(r) = \frac{T(r)}{n_e(r)^{\frac{2}{3}}} \cdot \tag{15}$$

This entropy corresponds to the heat supplied per particle for a given reference density. Figure 10 shows the entropy distribution as a function of radius, where the diamonds represent the entropy obtained from the spectra fitting results and the solid line from the best-fit function $T(r)$ and $n_e(r)$ profiles.

Pratt et al. (2006) demonstrated that the $S - T$ relation measured for 10 local and relaxed clusters observed by *XMM-Newton*, implies that $S_{0.3} \propto T_X^{0.64}$, where $S_{0.3}$ represents the entropy at $0.3r_{200}$ and T_X is the mean temperature in the region of $0.1r_{200} < r < 0.5r_{200}$. For RXC J2228.6+2036, $S_{0.3r200} = 959 \pm 130$ keV cm^2 and $T_X = 8.91^{+1.91}_{-1.33}$ keV. The $S_{0.3r200}$ versus T_X for RXC J2228.6+2036 is plotted on the $S - T$ relation derived by Pratt et al. (2006), shown in Fig. 11. The diamonds and the best-fit function (the solid line) are from Pratt et al. (2006), and the star indicates the measurement for RXC J2228.6+2036. It shows that our entropy value for

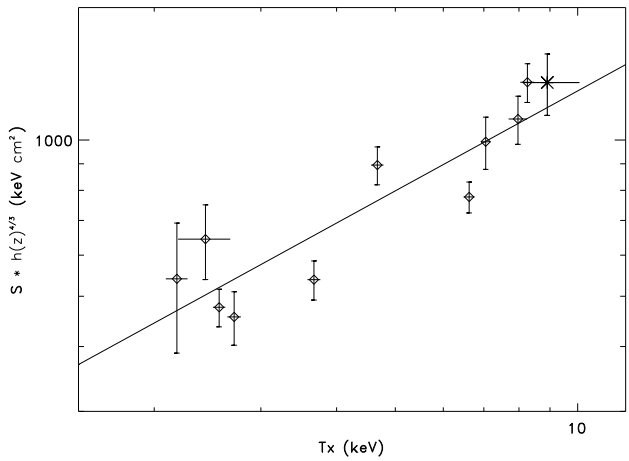

Fig. 11. Comparison of the present result with the $S - T$ relation of Pratt et al. (2006). The star indicates the result of RXC J2228.6+2036, and the diamonds and the best-fit $S - T$ relation line (the solid line) come from Pratt et al. (2006). Here, $h(z) = [0.3(1+z)^3 + 0.7]^{\frac{1}{2}}$. The error bars of the star are at the 68% confidence level.

RXC J2228.6+2036 is consistent (within the 1σ error bars) with the $S - T$ relation of Pratt et al. (2006) at $0.3r_{200}$, once corrected for the expected evolution in a self-similar scenario of structure formation.

5.4. M – T and L – T relations

From the above analysis, we derived the temperature, mass, and X-ray luminosity (see Table 1) of RXC J2228.6+2036: within $r_{500} = 4.8'$, $M_{500} = (1.19\pm0.35)\times10^{15}\,M_\odot$, $T_{500} = 8.92^{+1.78}_{-1.32}$ keV, and $L_{\rm bol,500} = 28.83^{+3.69}_{-4.78} \times 10^{44}$ erg s^{-1}. Therefore, we can compare RXC J2228.6+2036 to the empirical scaling relations for massive galaxy clusters, e.g. $M_{500} - T_{500}$ and $L_{\rm bol,500} - T_{500}$ derived from *XMM-Newton* data; examples of these scaling relations are those of Kotov & Vikhlinin (2005) based on 10 clusters at $z = 0.4$–0.7, Arnaud et al. (2005) based on 10 nearby clusters ($z < 0.15$), and Zhang et al. (2008) based on 37 LoCuSS

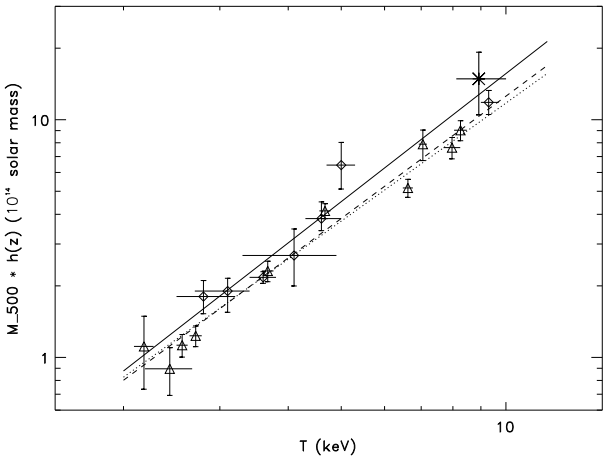

Fig. 12. Comparison of the present result with literature $M-T$ relations. The star indicates the result for RXC J2228.6+2036, the diamonds and their best-fitted $M-T$ relation line (the solid line) come from Kotov & Vikhlinin (2005), the triangles and the dashed line from Arnaud et al. (2005), and the dotted line from Zhang et al. (2008). Here, $h(z) = [0.3(1+z)^3 + 0.7]^{\frac{1}{2}}$. The error bars of the star represent the 68% confidence level.

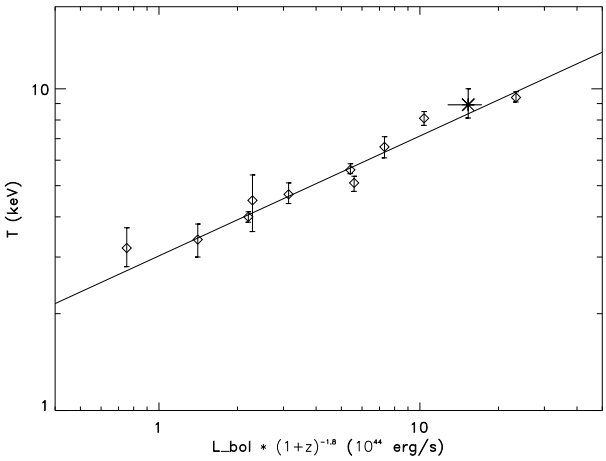

Fig. 13. Comparison of the present result with the $L-T$ relation of Kotov & Vikhlinin (2005). The star indicates the result of RXC J2228.6+2036, and the diamonds and the best-fit $L-T$ relation line (the solid line) come from Kotov & Vikhlinin (2005). The error bars of the star represent the 68% confidence level.

clusters at $z \sim 0.2$. The comparison of all relations is shown in Figs. 12, 13. The diamonds and the solid line are from Kotov & Vikhlinin (2005), the triangles and the dashed line from Arnaud et al. (2005), the dotted line from Zhang et al. (2008), and the star indicates the result of RXC J2228.6+2036.

It shows that our result is consistent with any of these previous studies within the scatter of the relations. The agreement of our $L-T$ relation with that of Kotov & Vikhlinin (2005, with objects in the same redshift range as ours) is remarkable, particularly because X-ray luminosity, with its square dependence on density, is a parameter that is sensitive to morphological disturbances and generally shows large scatter.

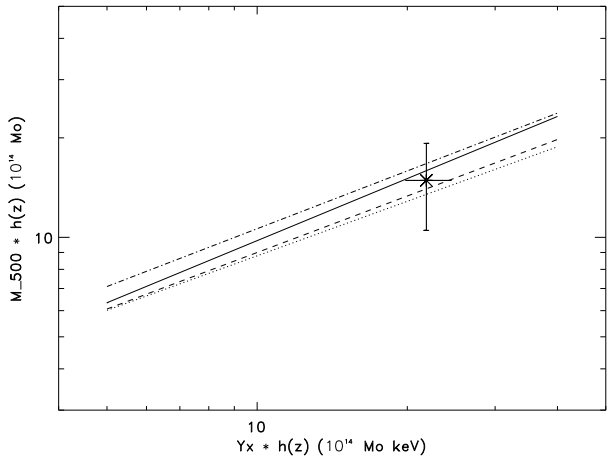

Fig. 14. Comparison of the present result with the $M-Y$ relation of Zhang et al. (2008) (the solid line), Kravtsov et al. (2006) (the dash-dotted line), Nagai et al. (2007) (the dashed line), and Arnaud et al. (2007) (the dotted line). The star indicates the result of RXC J2228.6+2036 with the errors of the 68% confidence level. $h(z) = [0.3(1+z)^3 + 0.7]^{\frac{1}{2}}$.

5.5. M – Y relation

The integrated SZ flux $Y_{\rm SZ} \propto \int k_{\rm B} T n_{\rm e} {\rm d}V \propto M_{\rm gas} T$, and thus the simplest X-ray analog is defined to be $Y_{\rm X} = M_{\rm gas} T$. Kravtsov et al. (2006) showed that $Y_{\rm X}$ is the best mass proxy with a remarkably low scatter and the $M - Y_{\rm X}$ relation is close to the self-similar prediction.

For RXC J2228.6+2036, $M_{500} = (1.19 \pm 0.35) \times 10^{15}\ M_\odot$ and $Y_{\rm X,500} = 21.84^{+2.70}_{-2.04} \times 10^{14}\ M_\odot$ keV. We plot M_{500} versus $Y_{\rm X}$ in Fig. 14 (shown as a star) and compare these data with the $M-Y_{\rm X}$ relations of Zhang et al. (2008) (the solid line), Kravtsov et al. (2006) (the dash-dotted line), Nagai et al. (2007) (the dashed line), and Arnaud et al. (2007) (the dotted line), which all show good consistency with our results.

6. Conclusion

We have presented a detailed analysis of the *XMM-Newton* observations of the distant galaxy cluster RXC J2228.6+2036 ($z = 0.421$) using our deprojection technique. By spectral fitting we obtained the deprojected temperature profile $T(r)$. Weighted by normalizations, we derived a mean temperature within r_{500} of $T_{500} = 8.92^{+1.78}_{-1.32}$ keV, which confirms, within the margins of error, the previous results of Pointecouteau et al. (2002) and LaRoque et al. (2006).

We then calculated the cooling time of this cluster and obtained a cooling radius of 147 ± 10 kpc. Fitted by a cooling flow model with an isothermal Mekal component, we derived the mass deposition rate $\sim 12.0^{+56.0}_{-12.0}\ M_\odot\ {\rm yr}^{-1}$ within $r_{\rm cool}$.

Using the radial density profile $n_{\rm e}(r)$ and radial temperature profile $T(r)$, we obtained the mass distribution of RXC J2228.6+2036. At $r_{500} = 1.61 \pm 0.16$ Mpc, the total mass is $M_{500} = (1.19 \pm 0.35) \times 10^{15}\ M_\odot$, in agreement with the results of Pointecouteau et al. (2002), derived from a combined SZ/X-ray spatial analysis, and the gas mass fraction is $f_{\rm gas} = 0.165 \pm 0.045$.

We discussed the PSF-correction effect on the spectral analysis and found that the PSF-corrected temperatures were consistent with those without PSF correction.

We found remarkable agreement, within the margins of error between our X-ray results and the SZ measurements of Pointecouteau et al. (2002), which is of prime importance to

future SZ surveys. The X-ray total mass and X-ray observables for RXC J2228.6+2036 closely obey the empirical scaling relations found in general massive galaxy clusters, e.g. the S–T, M–T, L–T, and M–Y relations, after accounting for self-similar evolution.

Acknowledgements. We thank G. Pratt for providing useful suggestions. This work was supported by CAS-MPG exchange program. S.M.J. acknowledges support from National Basic Research Program of China 2009CB824800. H.B. and E.P. acknowledge support by the DFG for the Excellence Cluster Universe, EXC 153. E.P. acknowledges the support of grant ANR-06-JCJC-0141. Y.Y.Z. acknowledges support from the German BMBF through the Verbundforschung under grant No. 50 OR 0601.

References

Arnaud, K. A. 1996, Astronomical Data Analysis Software and Systems V, ed. Jacoby G., & Barnes, J., ASP Conf. Ser., 101, 17
Arnaud, M., Majerowicz S., Lumb D., et al. 2002, A&A, 390, 27
Arnaud, M., Pointecouteau, E., & Pratt, G. W. 2005, A&A, 441, 893
Arnaud, M., Pointecouteau, E., & Pratt, G. W. 2006, A&A, 474, 37
Böhringer, H., Voges, W., Huchra, J. P., et al. 2000, ApJS, 129, 435
Böhringer, H., Matsushita, K., Churazov, E., Ikebe, Y., & Chen, Y. 2002, A&A, 382, 804
Chen, Y., Ikebe, Y., & Böhringer, H. 2003, A&A, 407, 41
Chen, Y., Reiprich, T. H., Böhringer, H., et al. 2007, A&A, 466, 805
De Luca, A., & Molendi, S. 2004, A&A, 419, 837
Dickey, J. M., & Lockman, F. J. 1990, ARA&A, 28, 215
Ebeling, H., Edge, A. C., Allen, S. W., et al. 2000, MNRAS, 318, 333
Ettori, S., Fabian, A. C., Allen, S. W., & Johnstone, R. M. 2002, MNRAS, 331, 635
Fabian, A. C. 1988, Science, 242, 1586
Fabricant, D., Lecar, M., & Gorenstein, P. 1980, ApJ, 241, 552
Gastaldello, F. A., Buote, D. A., Brighenti, F., & Mathews, W. G. 2007, [arXiv:0712.0783]
Ghizzardi, S. 2001, In-flight calibration of the PSF for MOS1 and MOS2 cameras, EPIC-MCT-TN-011, Internal report
Jia, S. M., Chen, Y., Lu, F. J., Chen, L., & Xiang, F. 2004, A&A, 423,65
Jia, S. M., Chen, Y., & Chen, L. 2006, ChJAA, 6, 181
Kaastra, J. S. 1992, An X-ray Spectral Code for Optically Thin Plasma Internal Sron-Leiden Report, updated version 2.0
Kotov, O., & Vikhlinin, A. 2005, ApJ, 633, 781
Kravtsov, A. V., Vikhlinin, A., & Nagai, D. 2006, ApJ, 650, 128
LaRoque, S. J., Bonamente, M., Carlstrom, J. E., et al. 2006, ApJ, 652, 917
Liedahl, D. A., Osterheld, A. L., & Goldstein, W. H. 1995, ApJ, 438, L115
Matsushita, K., Belsole, E., Finoguenov, A., & Böhringer, H. 2002, A&A, 386, 77
Mazzotta, P., Rasia, E., Moscardini, L., & Tormen, G. 2004, MNRAS, 354, 10
Mewe, R., Gronenschild, E. H. B. M., & van den Oord, G. H. J. 1985, A&AS, 62, 197
Mewe, R., Lemen, J. R., & van den Oord, G. H. J. 1986, A&AS, 65, 511
Morandi, A., Ettori, S., & Moscardini, L. 2007, MNRAS, 379, 518
Morrison, R., & McCammon, D. 1983, ApJ, 270, 119
Ngai, D., Kravtsov, A. V., & Vikhlinin, A. 2007, ApJ, 668, 1
Nulsen, P. E. J., & Böhringer, H. 1995, MNRAS, 274, 1093
Peterson, J. R., Kahn, S. M., Paerels, F. B. S., et al. 2003, ApJ, 590, 207
Pointecouteau, E., Giard, M., & Barret, D. 1998, A&A, 336, 44
Pointecouteau, E., Hattori, M., Neumann, D., et al. 2002, A&A, 387, 56
Pointecouteau, E., Arnaud, M., Kaastra, J., & de Plaa, J. 2004, A&A, 423, 33
Ponman, T. J., Cannon, D. B., & Navarro, J. F. 1999, Nature, 397, 135
Pratt, G. W., & Arnaud, M. 2002, A&A, 394, 375
Pratt, G. W., Arnaud, M., & Pointecouteau, E. 2006, A&A, 446, 429
Schuecker, P., Böhringer, H., Collins, C. A., & Guzzo, L. 2003, A&A, 398, 867
Snowden, S. L., Egger, R., Freyberg, M. J., et al. 1997, ApJ, 485, 125
Spergel, D. N., Verde, L., Peiris, H. V., et al. 2003, ApJ, 593, 705
Strüder, L., Briel, U., Dennerl, K., et al. 2001, A&A, 365, L18
Sunyaev, R., & Zel'dovich, Y. 1972, Comm. Astrophys. Space Phys., 4, 173
Vikhlinin, A. 2006, ApJ, 640, 710
White, D. A., Jones, C., & Forman, W. 1997, MNRAS, 292, 419
Xue, Y. J., Böhringer, H., & Matsushita, K. 2004, A&A, 420, 833
Zhang, Y. Y., Böhringer, H., Finoguenov, A., et al. 2006, A&A, 2006, 456, 55
Zhang, Y. Y., Finoguenov, A., Böhringer, H., et al. 2007, A&A, 467, 437
Zhang, Y. Y., Finoguenov, A., Böhringer, H., et al. 2008, [arXiv:0802.0770]